

Weyl-point teleportation

György Frank^{1,2}, Dániel Varjas³, Gergő Pintér^{1,2} and András Pályi^{1,2}

¹*Department of Theoretical Physics, Budapest University of Technology and Economics, Hungary*

²*MTA-BME Exotic Quantum Phases Group, Budapest University of Technology and Economics, Hungary*

³*Department of Physics, Stockholm University, AlbaNova University Center, 106 91 Stockholm, Sweden*

(Dated: August 8, 2022)

In this work, we describe the phenomenon of Weyl-point teleportation. Weyl points usually move continuously in the configuration parameter space of a quantum system when the control parameters are varied continuously. However, there are special transition points in the control space where the continuous motion of the Weyl points is disrupted. In such transition points, an extended nodal structure (nodal line or nodal surface) emerges, serving as a wormhole for the Weyl points, allowing their teleportation in the configuration space. A characteristic side effect of the teleportation is that the motional susceptibility of the Weyl point diverges in the vicinity of the transition point, and this divergence is characterized by a universal scaling law. We exemplify these effects via a two-spin model and a Weyl Josephson circuit model. We expect that these effects generalize to many other settings including electronic band structures of topological semimetals.

Introduction. Electronic band structures of crystalline materials often exhibit band touching points [1–3], leading to characteristic phenomena such as surface Fermi arcs [4], chiral anomaly, anomalous Hall effect, quantum oscillations, and quantized circular photogalvanic effect [5, 6]. The generic pattern for band touching is the Weyl point, where the dispersion relation in the vicinity of the degeneracy point starts linearly in all directions.

However, for many materials, the spatial symmetry of the crystal structure implies that band touching can happen in the form of extended nodal structures, such as nodal lines or nodal surfaces [7–21]. Furthermore, nodal lines and nodal surfaces can also arise in parameter-dependent quantum systems [22–24] in the presence of fine-tuning or symmetries. For brevity, we will use ‘fine-tuned’ to describe both of these scenarios.

Generic perturbations with respect to the fine-tuned setting will necessarily dissolve the extended nodal structures into a number of Weyl points. For example, mechanical strain can break the symmetry of a crystal and thereby split a nodal line into Weyl points [14]. Details of such a dissolution process have various physical implications, e.g., a qualitative change in the density of states and the properties of the surface states, etc. In this work we uncover general properties of this dissolution process.

In the above setting, the six independent components of the mechanical strain tensor provide examples of *control parameters*. We will refer to the fine-tuned control parameter point where the extended nodal structure appears as the *transition point*. Furthermore, we will call the parameter space in which the degeneracy structures live, i.e., the three-dimensional momentum space in the above example, the *configuration space*.

In this work, our main observation is that a nodal loop or nodal surface emerging at a transition point can be thought of as a ‘wormhole’ for Weyl points, allowing for the ‘teleportation’ of Weyl points. A side effect of teleportation is that the motion of the Weyl points become singular as the control parameters approach the transition point: an infinitesimal change in the control param-

eters induces a macroscopic displacement of the Weyl point in the configuration space.

Teleportation of magnetic Weyl points of a spin-orbit-coupled double quantum dot. We illustrate Weyl-point teleportation using an elementary model of a two-electron double quantum dot with spin-orbit interaction. The setup is shown in Fig. 1a. It consists of a cylindrically symmetric semiconducting nanowire (blue) where gate electrodes create a double-well potential (solid red), with each well capturing a single spinful electron (red clouds). The two localized spins interact with each other via exchange interaction.

We assume that an external homogeneous electric field $\mathbf{E} = (E_x, E_y, 0)$ breaks the cylindrical symmetry of the system, and induces an anisotropy in the Heisenberg interaction among the spins via the spin-orbit interaction of the Rashba type. The two-dimensional space of \mathbf{E} serves as the control space. A homogeneous external magnetic field \mathbf{B} is also present in the setup, taken into account by a Zeeman interaction term in the model. The three-dimensional space of \mathbf{B} serves as the configuration space.

The two-electron system is described by the following 4×4 Hamiltonian:

$$\hat{H}_{\text{DD}} = g\mu_B \mathbf{B} \cdot (\hat{\mathbf{S}}_L + \hat{\mathbf{S}}_R) + J \hat{\mathbf{S}}_L \cdot R(\mathbf{E}) \hat{\mathbf{S}}_R. \quad (1)$$

Here $\hat{\mathbf{S}}_{L/R}$ is the spin operator of the left/right electron, g is the g -factor of the electrons, μ_B is the Bohr magneton, \mathbf{B} is the external magnetic field, J is the exchange interaction strength, and $R(\mathbf{E})$ is a 3×3 rotation matrix describing the effect of spin-orbit interaction on the exchange interaction [25, 26].

The exchange term in Eq. (1) can be derived from the Rashba spin-orbit Hamiltonian and the corresponding two-site Hubbard model. Here, we outline the simple physical picture that predicts the qualitative dependence of the rotation matrix R on the electric field \mathbf{E} . Assume that the electric field creates a spin-orbit term of the Rashba type, $H_{\text{so}} = \alpha \hat{\mathbf{S}} \cdot (\mathbf{E} \times \hat{\mathbf{p}})$ [27]. When an electron tunnels from the right dot to the left ($|\mathbf{p}\rangle - |\mathbf{e}_z\rangle$), it feels

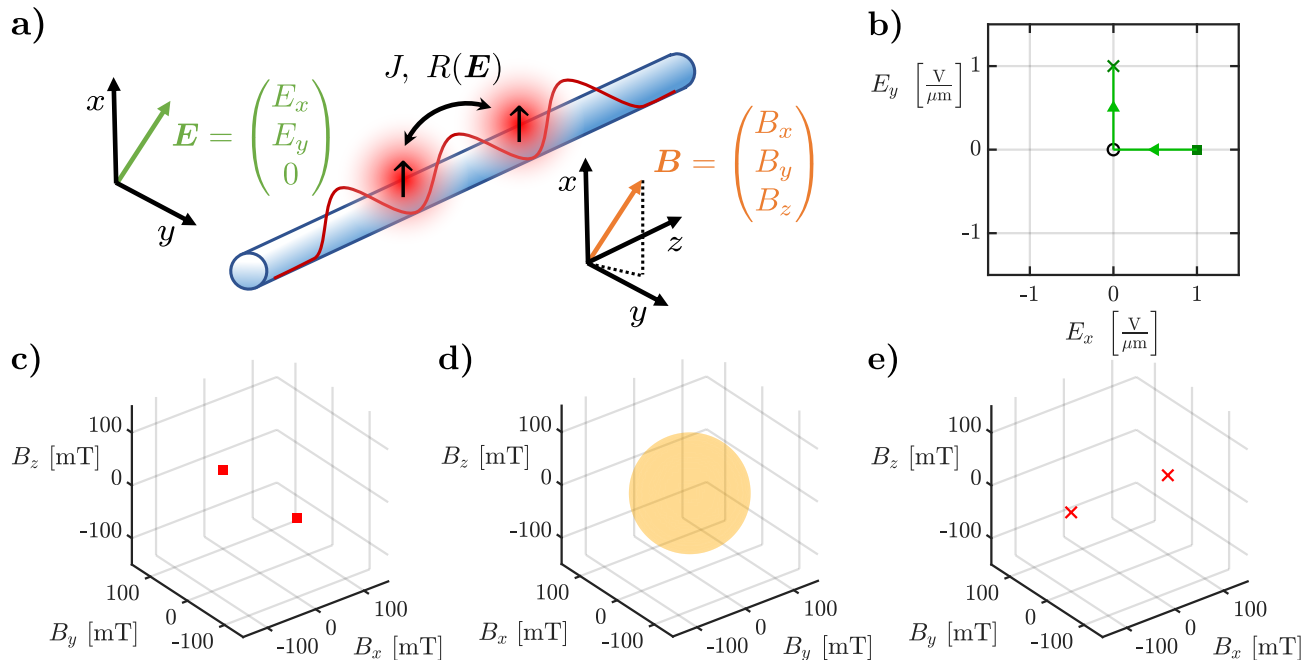


FIG. 1. **Teleportation of magnetic Weyl points of a spin-orbit-coupled double quantum dot.** (a) Double quantum dot hosting two interacting electrons, in the presence of a Zeeman field \mathbf{B} , and spin-orbit interaction induced by the electric field \mathbf{E} . (b) Trajectory of the control parameter vector, i.e., the electric field in the xy plane. The trajectory is parametrized by $t \in [-1, 1]$ with $\epsilon = 1V/\mu\text{m}$ (see text). (c,d,e) Evolution of ground-state Weyl points in the configuration space (\mathbf{B} space), as the control parameter vector is varied according to panel (b). Parameters: $g = 2$, $J = 11.6\mu\text{eV}$. (c) Weyl points for $t < 0$. (d) Nodal surface (sphere) at $t = 0$ (black circle in panel b). Teleportation of Weyl points happens at this point of the control-parameter trajectory. (e) Weyl points for $t > 0$.

a spin-orbit magnetic field $\mathbf{B}_{\text{so}} \propto \mathbf{e}_z \times \mathbf{E}$, and hence its spin rotates around \mathbf{B}_{so} with an angle $\theta = \gamma E$ proportional to the electric field causing the spin-orbit coupling. This effect is incorporated in Eq. (1) as the matrix R :

$$R(\mathbf{E}) = \exp \left[\gamma \begin{pmatrix} 0 & 0 & E_x \\ 0 & 0 & E_y \\ -E_x & -E_y & 0 \end{pmatrix} \right]. \quad (2)$$

Without spin-orbit interaction (that is, $\mathbf{E} = 0$), the system is isotropic. At zero magnetic field the ground state is a singlet, and the excited states are three degenerate triplets. Switching on an external magnetic field leaves the energy of the singlet state unchanged, but lowers the energy of one triplet state. At $B_0 = J/\mu_{gB}$ the ground state becomes degenerate. In the magnetic parameter space, the ground state degeneracy points form a nodal surface, i.e., a spherical surface with radius B_0 , see Fig. 1d.

With spin-orbit interaction ($\mathbf{E} \neq 0$), the ground state degeneracies split everywhere except the two points where the external magnetic field \mathbf{B} is parallel to the spin-orbit magnetic field \mathbf{B}_{so} . These two remaining degeneracy points are located at

$$\mathbf{B}_{W,\pm}(\mathbf{E}) = \pm B_0 \frac{\mathbf{e}_z \times \mathbf{E}}{E}, \quad (3)$$

where \mathbf{e}_z is the z -directional unit vector.

The above observations naturally combine into the Weyl-point teleportation effect, as illustrated by Fig. 1b-e. Consider the continuous trajectory of the control vector shown in Fig. 1b, parametrized by $t \in [-1, 1]$. This trajectory is defined as $\mathbf{E}(t) = -t\epsilon(1, 0, 0)$ for $t < 0$ and $\mathbf{E}(t) = t\epsilon(0, 1, 0)$ for $t \geq 0$, with $\epsilon > 0$ having the dimension of electric field. This trajectory contains the transition point $\mathbf{E}(0) = \mathbf{0}$. For $t < 0$, Weyl points are located in $\pm B_0 \mathbf{e}_y$ (panel b), whereas for $t > 0$, Weyl points are located in $\pm B_0 \mathbf{e}_x$ (panel e), and for $t = 0$ there are no Weyl points but a degeneracy sphere (panel d) that serves as a ‘wormhole’, allowing the ‘teleportation’ of the Weyl points as the control-space trajectory traverses the transition point.

Note that in our model, the Weyl points do not move ‘before’ ($t < 0$) and ‘after’ ($t > 0$) the teleportation. This changes in more realistic models, e.g., taking into account the electric-field dependence of the g -factor; see also our discussion on Weyl Josephson circuits below.

Divergence of motional susceptibility. Here, we exemplify that the motion of Weyl points in the configuration space is singular as the control parameters approach the transition point. We use the same two-spin model as above.

First, we introduce the *motional susceptibility matrix*

χ of a Weyl point, which is the quantity characterizing the motion of the Weyl point in configuration space in response to a small change of the control parameters. This matrix depends on the control parameters, and it is defined everywhere in the control space except in the transition point. For a selected Weyl point having the location $\mathbf{B}_W(\mathbf{E})$ in the configuration space (see, e.g., Eq. (3)), it is defined as

$$\chi_{ik}(\mathbf{E}) = \frac{\partial B_{W,i}(\mathbf{E})}{\partial E_k}, \quad (4)$$

where $i \in \{x, y, z\}$ and $k \in \{x, y\}$.

Hence for our two-spin model, this susceptibility matrix has dimension 3×2 . It can be obtained analytically from Eq. (3), e.g. by selecting the Weyl point $\mathbf{B}_{W,+}$, via the definition (4) as

$$\chi(\mathbf{E}) = \frac{B_0}{E^3} \begin{pmatrix} -E_x E_y & E_x^2 \\ -E_y^2 & E_x E_y \\ 0 & 0 \end{pmatrix}. \quad (5)$$

The singular value decomposition of this matrix has the form $\chi = U\Sigma V^T$, where

$$U(\mathbf{E}) = \frac{1}{E} \begin{pmatrix} -E_x & E_y & 0 \\ -E_y & -E_x & 0 \\ 0 & 0 & E \end{pmatrix} \quad (6)$$

$$\Sigma(\mathbf{E}) = \begin{pmatrix} \Sigma_1 & 0 \\ 0 & \Sigma_2 \\ 0 & 0 \end{pmatrix} \quad (7)$$

$$V(\mathbf{E}) = \frac{1}{E} \begin{pmatrix} -E_y & -E_x \\ E_x & -E_y \end{pmatrix} \quad (8)$$

Here, the two singular values are $\Sigma_1 = B_0/E$, $\Sigma_2 = 0$.

Remarkably, the largest singular value Σ_1 diverges as $1/E$ as the control parameters approach the transition point $\mathbf{E} = 0$. This shows that for paths that go close, but not through the transition point, an infinitesimal change of the control parameter yields a large movement of the Weyl point in the configuration space. This becomes a macroscopic jump when the path passes through the transition point and teleportation happens.

Weyl Josephson circuits. To show the generic nature of the effects discussed above, we now identify them in a different setup: a Weyl Josephson circuit [24]. The inset of Fig. 2a shows the schematic arrangement of a multi-terminal Josephson circuit, originally proposed in Fig. 1 of [24]. It is built from four superconducting terminals (black circles), where terminal 0 is grounded, and terminals 1, 2, and 3 are floating and controlled by local gate electrodes. The corresponding dimensionless gate voltages are denoted by $n_{g\alpha}$ with $\alpha \in \{1, 2, 3\}$. We regard these gate voltages as the control parameters. Furthermore, the three loops formed by the terminals, denoted as x, y, z in Fig. 2a, are pierced by controllable magnetic fluxes $\varphi_x, \varphi_y, \varphi_z$; we consider the 3D space of these fluxes as the configuration space. We denote the Josephson

energy (capacitance) associated to the junction between terminals α and β as $E_{J,\alpha\beta}$ ($C_{\alpha\beta}$).

The Hamiltonian of this Josephson circuit reads

$$\hat{H} = E_C (\hat{\mathbf{n}} - \mathbf{n}_g) \cdot c^{-1} (\hat{\mathbf{n}} - \mathbf{n}_g) - \sum_{\substack{\alpha,\beta=0 \\ \alpha<\beta}}^3 E_{J,\alpha\beta} \cos[\hat{\varphi}_\alpha - \hat{\varphi}_\beta + \gamma_{\alpha\beta}(\varphi_x, \varphi_y, \varphi_z)]. \quad (9)$$

Here, \hat{n}_α is the number operator counting the Cooper pairs on terminal $\alpha \in \{0, 1, 2, 3\}$, and $\hat{\mathbf{n}} = (\hat{n}_1, \hat{n}_2, \hat{n}_3)$. Furthermore, $\hat{\varphi}_\alpha$ are the phase operators canonically conjugated to \hat{n}_α , $E_C = (2e)^2/(2C_0)$ is a capacitance scale characteristic of the network of terminals, $c = C/C_0$ is the dimensionless capacitance matrix defined from the capacitance matrix [28] C (see Appendix), and $\gamma_{\alpha\beta}$ are control angles depending on the fluxes as $\gamma_{0\beta} = 0$, $\gamma_{12} = \varphi_x$, $\gamma_{13} = -\varphi_z$, and $\gamma_{23} = \varphi_y$.

If all three gate voltages $n_{g\alpha}$ have integer or half-integer values, then the Hamiltonian \hat{H} above has an effective time-reversal symmetry (see Appendix), implying that the ground-state degeneracy points, if they exist, form a loop in the configuration space. This is exemplified in Fig. 2 (a) and (b), where the black circle in panel (a) shows a gate-voltage vector with half-integer components, whereas the black solid loop in panel (b) shows the corresponding ground-state degeneracy pattern, i.e., a nodal loop. The black circle in panel (a) is a transition point, and the corresponding nodal loop is an extended degeneracy pattern, analogous to the sphere in the magnetic field space seen in Fig. 1c. The circuit parameters used to obtain this result are $(E_{J,01}, E_{J,02}, E_{J,03}, E_{J,12}, E_{J,13}, E_{J,23})/h = (2, 4, 6, 3, 3, 6)$ GHz, and $(C_{01}, C_{02}, C_{03}, C_{12}, C_{13}, C_{23})/h = (2, 1, 2, 3, 4, 3)$ fF. Furthermore, capacitances between terminals 1, 2, 3 and their respective control gates are $C_{g,1} = C_{g,2} = C_{g,3} = 0.1$ fF. (Numerical techniques used to obtain this result can be found in the Appendix.)

The nodal loop serves as a wormhole for the Weyl points, enabling their teleportation. This is illustrated in Fig. 2 (a) and (b). In (a), a continuous trajectory $\blacksquare \rightarrow \circ \rightarrow +$ including the transition point (\circ) is shown (green line). Here, the incoming and outgoing paths are straight, enclosing a finite angle. Formally, the trajectory in control space is defined as $\mathbf{n}_g(t) = \mathbf{n}_{g0} - t\mathbf{e}_\blacksquare$ for $t < 0$, $\mathbf{n}_g(t) = \mathbf{n}_{g0} + t\mathbf{e}_+$ for $t \geq 0$, with $\mathbf{e} = \mathbf{e}_\blacksquare = (3, 8, 6)/\sqrt{109}$, $\mathbf{e} = \mathbf{e}_+ = (3, 8, -6)/\sqrt{109}$, and $t \in [-0.1, 0.1]$. The corresponding motion of 4 ground-state Weyl points in the configuration space is shown in (b), where the red (blue) color denotes the $+1$ (-1) topological charge (ground-state Chern number) of the Weyl point. Even though the path in the control space is continuous (Fig. 2a), the Weyl-point positions in the configuration space suffer a sudden jump as the control-space trajectory crosses the transition point (Fig. 2b).

In the two-spin model described above, we have demonstrated the $1/E$ divergence of motional susceptibility of the Weyl points. We now identify the same type

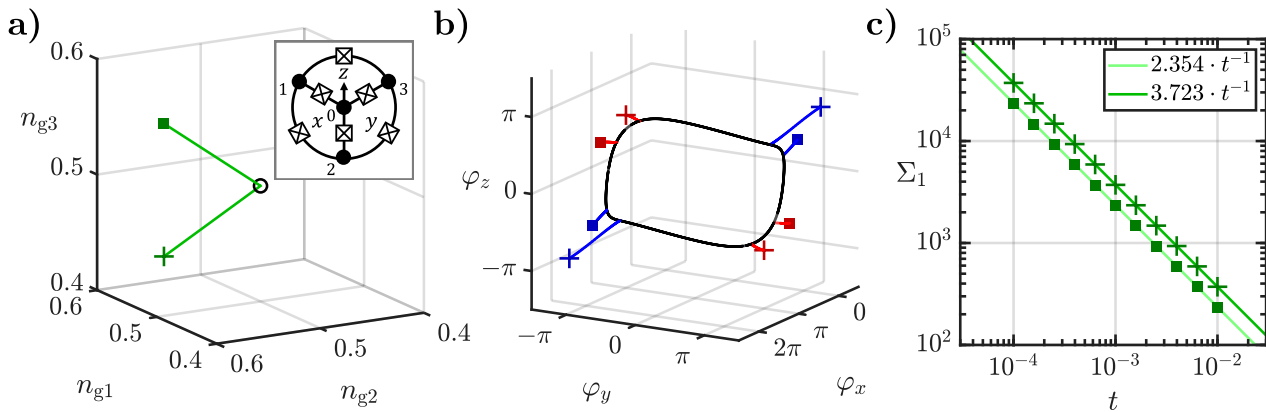


FIG. 2. **Weyl points and their teleportation in a Weyl Josephson circuit.** (a) Continuous trajectory $\blacksquare \rightarrow \circ \rightarrow +$ of the control parameter vector, i.e., the vector \mathbf{n}_g of gate voltages that controlling the Weyl Josephson circuit proposed in [24] (inset). (b) Evolution of four Weyl points in the configuration space, i.e., the space of the flux vector $\boldsymbol{\varphi}$, as the control parameter is varied on the path $\blacksquare \rightarrow \circ \rightarrow +$ in (a). Teleportation of the Weyl points happens at $\mathbf{n}_g = (0.5, 0.5, 0.5)$, marked by the black circle in (a), when the degeneracy points in the configuration space form a nodal loop (black) in panel (b). See text for parameters. (c) Scaling of Weyl-point motion in a Weyl Josephson circuit. The greatest singular value Σ_1 of the motional susceptibility matrix χ exhibits a $1/t$ divergence as the control vector approaches the transition point as $\mathbf{n}_g(t) = \mathbf{n}_{g0} + t\mathbf{e}$. The two data sets correspond to $\mathbf{e} = \mathbf{e}_\blacksquare$ and $\mathbf{e} = \mathbf{e}_+$ (see text), and the motion of the top left Weyl point in panel b). The straight lines in c) are single-parameter fits to the data, see inset.

of divergence in this Weyl Josephson circuit model, using the results in Fig. 2c. For each of the two directions of Fig. 2a, i.e., the ones denoted by the green square and the green cross, we numerically compute the greatest singular value of the motional susceptibility matrix of a selected Weyl point as the control vector is changed according to $\mathbf{n}_g(t) = \mathbf{n}_{g0} + t\mathbf{e}$ with $t \in [10^{-4}, 0.01]$, for two cases: $\mathbf{e} = \mathbf{e}_\blacksquare$ and $\mathbf{e} = \mathbf{e}_+$. Figure 2c shows the obtained data points, along with the two single-parameter fits to the data (solid lines). These results reveal that in the vicinity of the transition point (that is, for $t \rightarrow 0$), all of these singular values show a $1/t$ divergence. We have checked that this behavior holds for all Weyl points created from the nodal loop, for various Hamiltonian parameter values and directions in control space.

Based on our results for the two-spin model and the Weyl Josephson circuit model, we conjecture that this $1/t$ divergence of Weyl-point motional susceptibility is a generic feature in the vicinity of a nodal loop and a nodal surface, irrespective of the specific physical setup. We pose it as an open problem to rigorously identify the preconditions of this scaling law.

In fact, the divergent motional susceptibility of the Weyl points in the vicinity of the nodal surface or nodal line can be regarded as a side effect of teleportation. A simple argument is as follows. Consider a circular path connecting the control points $\mathbf{n}_{g0} + t\mathbf{e}_\blacksquare$ and $\mathbf{n}_{g0} + t\mathbf{e}_+$, centered around the transition point \mathbf{n}_{g0} . The path length approaches zero as $t \rightarrow 0$, being proportional to t . We compare this with the corresponding Weyl-point path length in the configuration space, by inspecting, e.g., the top left Weyl point in Fig. 2b. The Weyl-point path

length does not converge to zero as $t \rightarrow 0$; instead, it converges to the path length between the meeting points of the Weyl-point trajectory and the nodal loop (i.e., the *teleportation length*), which is finite. This simple consideration explains that in the vicinity of the transition point, a small generic change in the control vector implies a large jump of the Weyl points; furthermore, it provides an interpretation of the $1/t$ type divergence of the motional susceptibility.

Conclusions. In conclusion, we have argued that nodal loops and nodal surfaces of parameter-dependent quantum systems serve as wormholes for Weyl points, allowing their teleportation. Furthermore, as the control parameters approach the transition point where the degeneracy points form a loop or a surface, the pace of motion of the Weyl points in the configuration space diverges, following a simple scaling law. A special case of the teleportation effect was found in superfluid $^3\text{He-A}$ [29] where two oppositely charged Weyl points switch places through a nodal loop. We exemplified more general teleportation patterns on a two-spin model and a Weyl Josephson circuit, and we expect that they generalize naturally to many other settings, including electronic [3, 11, 14, 19, 30], photonic [31, 32], phononic [33], magnonic [34], and synthetic [35] band structures.

Author contributions. Gy. F. performed analytical and numerical calculations, and produced the figures. Gy. F. and A. P. wrote the initial draft of the manuscript. A. P. acquired funding, and managed the project. G. P. consulted on differential-geometric aspects of the work. All authors contributed to the formulation of the project, discussed the results and took part in writing the

manuscript.

ACKNOWLEDGMENTS

We acknowledge fruitful discussions and correspondence with J. Asbóth, L. Bretheau, V. Fatemi, Y. Qian, A. Schnyder, and H. Weng. This research was supported by the Ministry of Innovation and Technology (MIT) and

the National Research, Development and Innovation Office (NKFIH) within the Quantum Information National Laboratory of Hungary and the Quantum Technology National Excellence Program (Project No. 2017-1.2.1-NKP-2017-00001), by the NKFIH fund TKP2020 IES (Grant No. BME-IE-NAT) under the auspices of the MIT, and by the NKFIH through the OTKA Grants FK 124723 and FK 132146. D. V. was supported by the Swedish Research Council (VR) and the Knut and Alice Wallenberg Foundation.

-
- [1] J. von Neumann and E. P. Wigner, Über das Verhalten von Eigenwerten bei adiabatischen Prozessen, *Physikalische Zeitschrift* **30**, 467 (1929).
- [2] C. Herring, Accidental degeneracy in the energy bands of crystals, *Phys. Rev.* **52**, 365 (1937).
- [3] N. P. Armitage, E. J. Mele, and A. Vishwanath, Weyl and Dirac semimetals in three-dimensional solids, *Rev. Mod. Phys.* **90**, 015001 (2018).
- [4] S.-M. Huang, S.-Y. Xu, I. Belopolski, C.-C. Lee, G. Chang, B. Wang, N. Alidoust, G. Bian, M. Neupane, C. Zhang, S. Jia, A. Bansil, H. Lin, and M. Z. Hasan, A Weyl Fermion semimetal with surface Fermi arcs in the transition metal monpnictide TaAs class, *Nature Communications* **6**, 7373 (2015).
- [5] F. de Juan, A. G. Grushin, T. Morimoto, and J. E. Moore, Quantized circular photogalvanic effect in Weyl semimetals, *Nature Communications* **8**, 15995 (2017).
- [6] Q. Ma, S.-Y. Xu, C.-K. Chan, C.-L. Zhang, G. Chang, Y. Lin, W. Xie, T. Palacios, H. Lin, S. Jia, P. Lee, P. Jarillo-Herrero, and N. Gedik, Direct optical detection of Weyl fermion chirality in a topological semimetal, *Nature Physics* **13** (2017).
- [7] B. Béri, Topologically stable gapless phases of time-reversal-invariant superconductors, *Phys. Rev. B* **81**, 134515 (2010).
- [8] J.-M. Carter, V. V. Shankar, M. A. Zeb, and H.-Y. Kee, Semimetal and topological insulator in perovskite iridates, *Phys. Rev. B* **85**, 115105 (2012).
- [9] C. Fang, Y. Chen, H.-Y. Kee, and L. Fu, Topological nodal line semimetals with and without spin-orbital coupling, *Phys. Rev. B* **92**, 081201 (2015).
- [10] W. Wu, Y. Liu, S. Li, C. Zhong, Z.-M. Yu, X.-L. Sheng, Y. X. Zhao, and S. A. Yang, Nodal surface semimetals: Theory and material realization, *Phys. Rev. B* **97**, 115125 (2018).
- [11] C. Fang, H. Weng, X. Dai, and Z. Fang, Topological nodal line semimetals, *Chinese Physics B* **25**, 117106 (2016).
- [12] T. Bzdušek, Q. Wu, A. Rüegg, M. Sigrist, and A. A. Soluyanov, Nodal-chain metals, *Nature* **538**, 75 (2016).
- [13] Q.-F. Liang, J. Zhou, R. Yu, Z. Wang, and H. Weng, Node-surface and node-line fermions from nonsymmorphic lattice symmetries, *Phys. Rev. B* **93**, 085427 (2016).
- [14] Y.-M. Xie, X.-J. Gao, X. Y. Xu, C.-P. Zhang, J.-X. Hu, J. Z. Gao, and K. T. Law, Kramers nodal line metals, *Nature Communications* **12**, 3064 (2021).
- [15] Y. Zhao and A. P. Schnyder, Nonsymmorphic symmetry-required band crossings in topological semimetals, *Physical Review B* **94**, 195109 (2016).
- [16] J. Zhang, Y.-H. Chan, C.-K. Chiu, M. G. Vergniory, L. M. Schoop, and A. P. Schnyder, Topological band crossings in hexagonal materials, *Physical Review Materials* **2**, 074201 (2018).
- [17] Y.-H. Chan, B. Kilic, M. M. Hirschmann, C.-K. Chiu, L. M. Schoop, D. G. Joshi, and A. P. Schnyder, Symmetry-enforced band crossings in trigonal materials: Accordion states and Weyl nodal lines, *Physical Review Materials* **3**, 124204 (2019).
- [18] M. M. Hirschmann, A. Leonhardt, B. Kilic, D. H. Fabini, and A. P. Schnyder, Symmetry-enforced band crossings in tetragonal materials: Dirac and Weyl degeneracies on points, lines, and planes, *Phys. Rev. Materials* **5**, 054202 (2021).
- [19] M. A. Wilde, M. Dodenhöft, A. Niedermayr, A. Bauer, M. M. Hirschmann, K. Alpin, A. P. Schnyder, and C. Pfleiderer, Symmetry-enforced topological nodal planes at the Fermi surface of a chiral magnet, *Nature* **594**, 374 (2021).
- [20] R. González-Hernández, E. Tuiran, and B. Uribe, Topological electronic structure and Weyl points in nonsymmorphic hexagonal materials, *Phys. Rev. Materials* **4**, 124203 (2020).
- [21] S.-Y. Yang, H. Yang, E. Derunova, S. Parkin, B. Yan, and M. Ali, Symmetry demanded topological nodal-line materials, *Advances in Physics: X* **3** (2017).
- [22] G. Frank, Z. Scherübl, S. Csonka, G. Zaránd, and A. Pályi, Magnetic degeneracy points in interacting two-spin systems: Geometrical patterns, topological charge distributions, and their stability, *Physical Review B* **101**, 245409 (2020).
- [23] G. Frank, D. Varjas, P. Vrana, G. Pintér, and A. Pályi, arXiv:2012.14357 (unpublished).
- [24] V. Fatemi, A. R. Akhmerov, and L. Bretheau, Weyl Josephson circuits, *Phys. Rev. Research* **3**, 013288 (2021).
- [25] K. V. Kavokin, Symmetry of anisotropic exchange interactions in semiconductor nanostructures, *Phys. Rev. B* **69**, 075302 (2004).
- [26] Z. Scherübl, A. Pályi, G. Frank, I. E. Lukács, G. Fülöp, B. Fülöp, J. Nygård, K. Watanabe, T. Taniguchi, G. Zaránd, and S. Csonka, Observation of spin-orbit coupling induced Weyl points in a two-electron double quantum dot, *Communications Physics* **2**, 108 (2019).
- [27] Z. Scherübl, G. Fülöp, M. H. Madsen, J. Nygård, and S. Csonka, Electrical tuning of Rashba spin-orbit interaction in multigated InAs nanowires, *Physical Review B* **94**, 035444 (2016).

- [28] W. G. van der Wiel, S. De Franceschi, J. M. Elzerman, T. Fujisawa, S. Tarucha, and L. P. Kouwenhoven, Electron transport through double quantum dots, *Rev. Mod. Phys.* **75**, 1 (2002).
- [29] J. Nissinen and G. Volovik, Dimensional crossover of effective orbital dynamics in polar distorted $^3\text{He-A}$: Transitions to antispacetime, *Physical Review D* **97**, 025018 (2018).
- [30] J. Li, H. Wang, and H. Pan, Tunable topological phase transition from nodal-line semimetal to weyl semimetal by breaking symmetry, *Physical Review B* **104**, 235136 (2021).
- [31] W. Gao, B. Yang, M. Lawrence, F. Fang, B. Béri, and S. Zhang, Photonic Weyl degeneracies in magnetized plasma, *Nature Communications* **7**, 12435 (2016).
- [32] B. Yang, Q. Guo, B. Tremain, R. Liu, L. E. Barr, Q. Yan, W. Gao, H. Liu, Y. Xiang, J. Chen, C. Fang, A. Hibbins, L. Lu, and S. Zhang, Ideal Weyl points and helicoid surface states in artificial photonic crystal structures, *Science* **359**, 1013 (2018).
- [33] F. Li, X. Huang, J. Lu, J. Ma, and Z. Liu, Weyl points and Fermi arcs in a chiral phononic crystal, *Nature Physics* **14**, 30 (2018).
- [34] J. Romhányi, K. Penc, and R. Ganesh, Hall effect of triplons in a dimerized quantum magnet, *Nature Communications* **6**, 6805 (2015).
- [35] R.-P. Riwar, M. Houzet, J. S. Meyer, and Y. V. Nazarov, Multi-terminal Josephson junctions as topological matter, *Nature Communications* **7**, 11167 (2016).

Appendix A: Exchange rotation in the interacting two-spin model

Here, we provide a heuristic estimate for the exchange rotation angle γE included in the interacting two-spin model of the main text.

The exchange interaction in Eq. (2) contains a rotation matrix of angle γE . To estimate γ in a realistic setting, we consider electrons in an InAs nanowire ($m_{\text{eff}} = 0.023 m_e$), subject to an electric field that is assumed to be homogeneous. We identify the exchange rotation angle with the spin rotation angle via

$$\gamma E = 2\pi \ell_d / \ell_{\text{so}} \quad (\text{A1})$$

of a free conduction electron in the nanowire as it traverses the interdot distance ℓ_d of the double quantum dot system. The spin-orbit length ℓ_{so} , according to [27], can be expressed as

$$\ell_{\text{so}} = \frac{\hbar^2}{m_{\text{eff}} e \alpha_0 E}, \quad (\text{A2})$$

with $\alpha_0 = 1.17 \text{ nm}^2$.

The above relations imply

$$\gamma = \frac{2\pi \ell_d m_{\text{eff}} e \alpha_0}{\hbar^2} \approx 222 \text{ nm/V}, \quad (\text{A3})$$

where an interdot distance of $\ell_d = 100 \text{ nm}$ was used. That is, an electric field $E = 1 \mu\text{m/V}$ implies an exchange rotation of $\gamma E = 0.222$ radians, approximately 13 degrees.

Appendix B: The capacitance matrix of the Weyl Josephson circuit

The capacitance matrix [28] of the Weyl Josephson circuit described in the main text reads:

$$C = \begin{pmatrix} C_1 & -C_{12} & -C_{13} \\ -C_{12} & C_2 & -C_{23} \\ -C_{13} & -C_{23} & C_3 \end{pmatrix}, \quad (\text{B1})$$

where

$$C_1 = C_{01} + C_{12} + C_{13} + C_{g1}, \quad (\text{B2a})$$

$$C_2 = C_{02} + C_{12} + C_{23} + C_{g2}, \quad (\text{B2b})$$

$$C_3 = C_{03} + C_{13} + C_{23} + C_{g3}. \quad (\text{B2c})$$

Appendix C: Effective \mathcal{PT} symmetry protecting the nodal loops of the Weyl Josephson circuit

The Josephson-circuit Hamiltonian $\hat{H}(\mathbf{n}_g, \varphi)$ has time-reversal symmetry in the absence of magnetic fluxes:

$$\mathcal{T} \hat{H}(\mathbf{n}_g, 0) \mathcal{T}^{-1} = \hat{H}(\mathbf{n}_g, 0), \quad (\text{C1})$$

where $\mathcal{T} = \mathcal{K}$ is the complex conjugation in the charge basis [24], and hence $\mathcal{T}^2 = 1$. Furthermore, for nonzero magnetic flux, the relation (C1) generalizes as

$$\mathcal{T} \hat{H}(\mathbf{n}_g, \varphi) \mathcal{T}^{-1} = \hat{H}(\mathbf{n}_g, -\varphi). \quad (\text{C2})$$

In the charge basis, this is translated to

$$H_{\mathbf{n}, \mathbf{n}'}^*(\mathbf{n}_g, \varphi) = H_{\mathbf{n}, \mathbf{n}'}(\mathbf{n}_g, -\varphi). \quad (\text{C3})$$

Other symmetries of \hat{H} are charge inversion

$$H(\mathbf{n}_g, \varphi)_{\mathbf{n}, \mathbf{n}'} = H(-\mathbf{n}_g, -\varphi)_{-\mathbf{n}, -\mathbf{n}'}, \quad (\text{C4})$$

and discrete charge translation symmetry

$$H(\mathbf{n}_g, \varphi)_{\mathbf{n}, \mathbf{n}'} = H(\mathbf{n}_g + \mathbf{m}, \varphi)_{\mathbf{n} + \mathbf{m}, \mathbf{n}' + \mathbf{m}} \quad (\text{C5})$$

where \mathbf{m} is an arbitrary integer offset charge vector.

The charge inversion and charge translation together gives

$$H(\mathbf{n}_g, \varphi)_{\mathbf{n}, \mathbf{n}'} = H(\mathbf{m} - \mathbf{n}_g, -\varphi)_{\mathbf{m} - \mathbf{n}, \mathbf{m} - \mathbf{n}'}. \quad (\text{C6})$$

This relation implies that for fixed integer or a half-integer offset charge vector $\mathbf{n}_g = \frac{\mathbf{m}}{2}$, it holds that

$$H\left(\frac{\mathbf{m}}{2}, \varphi\right)_{\mathbf{n}, \mathbf{n}'} = H\left(\frac{\mathbf{m}}{2}, -\varphi\right)_{\mathbf{m} - \mathbf{n}, \mathbf{m} - \mathbf{n}'}. \quad (\text{C7})$$

This relation can be expressed by the charge inversion operator $\mathcal{P}^{(\mathbf{m}/2)}$, whose matrix elements in the charge basis are

$$P_{\mathbf{n}, \mathbf{n}'}^{(\mathbf{m}/2)} = \delta_{\mathbf{n}, \mathbf{m} - \mathbf{n}'}. \quad (\text{C8})$$

With this definition, we rewrite Eq. (C7) as

$$\mathcal{P}^{(\mathbf{m}/2)} \hat{H}\left(\frac{\mathbf{m}}{2}, \varphi\right) \left(\mathcal{P}^{(\mathbf{m}/2)}\right)^{-1} = \hat{H}\left(\frac{\mathbf{m}}{2}, -\varphi\right). \quad (\text{C9})$$

inverting the charge with respect to $\frac{\mathbf{m}}{2}$. This is an exact symmetry even when the charge basis is restricted to a finite interval symmetrically around $\frac{\mathbf{m}}{2}$.

Henceforth, we fix the charge inversion point as $\frac{\mathbf{m}}{2}$, and suppress it in the formulas below. Then, the combination of charge inversion and time-reversal symmetry results in

$$(\mathcal{PT}) \hat{H}(\varphi) (\mathcal{PT})^{-1} = \hat{H}(\varphi), \quad (\text{C10})$$

i.e., we have identified an antiunitary symmetry \mathcal{PT} with $(\mathcal{PT})^2 = 1$ that restricts the Hamiltonian at every value of φ for a fixed $\mathbf{n}_g = \frac{\mathbf{m}}{2}$ integer or a half-integer offset charge vector. Carrying out a basis transformation from the charge basis by the unitary $U = \sqrt{\mathcal{P}}$, \mathcal{PT} is represented as complex conjugation, making the transformed $H(\varphi)$ real. The co-dimension for real valued symmetric matrices to be two-fold degenerate is 2 (see, e.g., Ref. [1]), meaning that the level crossings generally appear as 1 dimensional space curves in the 3 dimensional φ parameter space.

To show a specific example, we consider the truncated 8×8 Hamiltonian of the Josephson circuit in the charge basis

$\{|000\rangle, |100\rangle, |010\rangle, |001\rangle, |111\rangle, |011\rangle, |101\rangle, |110\rangle\}$, which reads

$$H_{8 \times 8}(\mathbf{n}_g, \boldsymbol{\varphi}) = \begin{pmatrix} \epsilon_{000} & h_{01} & h_{02} & h_{03} & 0 & 0 & 0 & 0 \\ h_{01} & \epsilon_{100} & h_{12}^* & h_{31} & 0 & 0 & h_{03} & h_{02} \\ h_{02} & h_{12} & \epsilon_{010} & h_{23}^* & 0 & h_{03} & 0 & h_{01} \\ h_{03} & h_{31}^* & h_{23} & \epsilon_{001} & 0 & h_{02} & h_{01} & 0 \\ 0 & 0 & 0 & 0 & \epsilon_{111} & h_{01} & h_{02} & h_{03} \\ 0 & 0 & h_{03} & h_{02} & h_{01} & \epsilon_{011} & h_{12} & h_{31}^* \\ 0 & h_{03} & 0 & h_{01} & h_{02} & h_{12}^* & \epsilon_{101} & h_{23} \\ 0 & h_{02} & h_{01} & 0 & h_{03} & h_{31} & h_{23}^* & \epsilon_{110} \end{pmatrix}, \quad (\text{C11})$$

where

$$\epsilon_{abc} = E_C[(a, b, c)^T - \mathbf{n}_g] \cdot c^{-1}[(a, b, c)^T - \mathbf{n}_g] \quad (\text{C12})$$

$$h_{\alpha\beta} = -\frac{1}{2} E_{J, \alpha\beta} e^{-i\gamma_{\alpha\beta}}. \quad (\text{C13})$$

At the time-reversal offset charge point $\mathbf{n}_g = (\frac{1}{2}, \frac{1}{2}, \frac{1}{2})^T \equiv \frac{1}{2}$, the diagonal elements have the property

$$\epsilon_{a,b,c} = \epsilon_{1-a, 1-b, 1-c}, \quad (\text{C14})$$

yielding the \mathcal{PT} symmetry

$$PH_{8 \times 8}^*(\boldsymbol{\varphi})P^{-1} = H_{8 \times 8}(\boldsymbol{\varphi}), \quad (\text{C15})$$

with $P = \sigma_x \otimes \mathbf{1}_{4 \times 4}$. The corresponding unitary matrix $U = \sqrt{i/2}(\mathbf{1}_{2 \times 2} - i\sigma_x) \otimes \mathbf{1}_{4 \times 4}$ transforms the Hamiltonian matrix to be real-valued

$$UH_{8 \times 8}(\boldsymbol{\varphi})U^{-1} = [UH_{8 \times 8}(\boldsymbol{\varphi})U^{-1}]^*. \quad (\text{C16})$$

Appendix D: Weyl Josephson circuit: Numerical techniques

The calculations of the Weyl Josephson circuits were done numerically, with the aid of analytical techniques. The starting point of the calculation was the truncated matrix representation of the Hamiltonian of Eq. (10) of the main text. The matrix representation was obtained by projecting the Hamiltonian onto the subspace spanned by the charge basis states $|n_1, n_2, n_3\rangle$, with $n_1, n_2, n_3 \in \{-1, 0, 1, 2\}$, yielding a $4^3 \times 4^3 = 64 \times 64$ matrix.

This charge interval is chosen to be symmetric to $1/2$, to respect the symmetry of Eq. (C10) protecting the nodal loop at $\mathbf{n}_{g0} = (0.5, 0.5, 0.5)$. The range of the charge states was chosen to be large enough to describe the physical system accurately, and small enough to save computational time.

To check the error due to the truncation of the Hamiltonian, we have compared the numerically identified nodal loops for smaller and larger matrix dimensions, see Fig. 3a. Besides the 64×64 truncation size, the figure shows results with the 8×8 and 216×216 Hamiltonians,

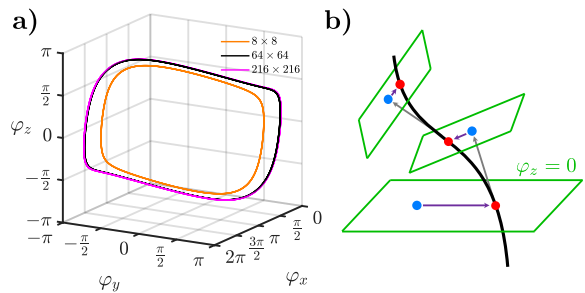


FIG. 3. Nodal loop in the Weyl Josephson junction. a) Numerical identification of nodal loops and Weyl points was carried out by truncating the infinite-dimensional Hilbert space of the Weyl Josephson circuit. Larger Hamiltonian matrices give more accurate results: the corresponding nodal loops converge. b) Numerical search for the points (red) of the nodal loop (black). The search consists of two nested iterations: the inner iteration (purple) searches for the intersection of the nodal loop with a plane (green). After the intersection is found, the outer iteration makes a step of a finite distance in the tangential direction of the nodal loop (grey) and determines the new searching plane as the perpendicular plane passing through the new point (blue). The first inner iteration searches in the $\varphi_z = 0$ plane.

corresponding to the charge ranges $0 \leq n_{1,2,3} \leq 1$ and $-2 \leq n_{1,2,3} \leq 3$, respectively. We found that all truncated Hamiltonians have the same qualitative behaviour, i.e., presence of nodal loop, Weyl point teleportation, and susceptibility divergence. Moreover, the quantitative difference between the results from the two larger Hamiltonians is negligible, e.g., the distance between the points of the nodal loops in the $\varphi_z = 0$ plane is 0.036 rad (see Fig. 3a).

In the following subsections, we present the numerical techniques for characterizing the nodal loop and searching for the Weyl points. We use a generic description where \mathbf{p} is the 3-component configurational parameter in the configurational space where the Weyl points and the nodal loop are present, and \mathbf{q} is the k -component control parameter which can tune system. The correspondence between this notation and the notation of gate voltages and magnetic fluxes in the Weyl Josephson circuit reads:

$$\mathbf{p} \equiv \boldsymbol{\varphi} = (\varphi_x, \varphi_y, \varphi_z), \quad (\text{D1})$$

$$\mathbf{q} \equiv \mathbf{n}_g = (n_{g,1}, n_{g,2}, n_{g,3}). \quad (\text{D2})$$

1. Effective 2×2 Hamiltonian near two-fold degeneracies

Searching for the degeneracies of a large Hamiltonian can be computationally demanding. To ease the problem, a useful technique is to reduce the Hamiltonian to a low-dimensional effective model with Schrieffer–Wolff transformation. Consider the Hamiltonian $H(\mathbf{p}, \mathbf{q})$ depending on the 3 dimensional configurational space \mathbf{p} and

the k dimensional \mathbf{q} control space. At $(\mathbf{p}_0, \mathbf{q}_0)$, the i th and $(i+1)$ th energies, to be denoted as $E_i(\mathbf{p}_0, \mathbf{q}_0)$ and $E_{i+1}(\mathbf{p}_0, \mathbf{q}_0)$, are close together and well separated from the other energy levels.

In our method to find a degeneracy point in the vicinity of such a quasi-degenerate point $(\mathbf{p}_0, \mathbf{q}_0)$, a useful ingredient is to expand the Hamiltonian in linear order as

$$H^{(1)}(\mathbf{p}_0 + \delta\mathbf{p}, \mathbf{q}_0 + \delta\mathbf{q}) = H(\mathbf{p}_0, \mathbf{q}_0) + \left. \frac{\partial H}{\partial \mathbf{p}} \right|_{\mathbf{p}_0, \mathbf{q}_0} \cdot \delta\mathbf{p} + \left. \frac{\partial H}{\partial \mathbf{q}} \right|_{\mathbf{p}_0, \mathbf{q}_0} \cdot \delta\mathbf{q}, \quad (\text{D3})$$

and project it to the subspace of the quasi-degenerate levels with $P_0 = |\Psi_i\rangle\langle\Psi_i| + |\Psi_{i+1}\rangle\langle\Psi_{i+1}|$, where $|\Psi_i\rangle$ and $|\Psi_{i+1}\rangle$ are the i th and $(i+1)$ th energy eigenstates of $H(\mathbf{p}_0, \mathbf{q}_0)$. This projection yields the following 2×2 effective Hamiltonian:

$$H_{\text{eff}}^{(1)} = P_0 H^{(1)} P_0 \equiv \boldsymbol{\sigma} \cdot \boldsymbol{\Delta}^{(1)} = \boldsymbol{\sigma} \cdot [\boldsymbol{\Delta}_0 + g_{\mathbf{p}} \delta\mathbf{p} + g_{\mathbf{q}} \delta\mathbf{q}]. \quad (\text{D4})$$

Here, $\boldsymbol{\sigma} = (\sigma_x, \sigma_y, \sigma_z)$ is the vector of Pauli operators acting on the quasi-degenerate subspace. We neglected the σ_0 term in the expansion, since because it does not affect the splitting between the two states.

By the above definition, the only nonzero component of the *polarization vector* $\boldsymbol{\Delta}_0$ is its third component. Furthermore, we call $g_{\mathbf{p}}$ and $g_{\mathbf{q}}$ as the configurational-space and control-space *effective g -tensors*, which are a real valued 3×3 and $3 \times k$ matrices:

$$\begin{aligned} [\boldsymbol{\Delta}_0(\mathbf{p}_0, \mathbf{q}_0)]_3 &= \frac{1}{2} [E_i(\mathbf{p}_0, \mathbf{q}_0) - E_{i+1}(\mathbf{p}_0, \mathbf{q}_0)], \\ [g_{\mathbf{p}}(\mathbf{p}_0, \mathbf{q}_0)]_{\alpha, \beta} &= \frac{1}{2} \text{Tr} \left(\sigma_{\alpha} P_0 \left. \frac{\partial H}{\partial p_{\beta}} \right|_{\mathbf{p}_0, \mathbf{q}_0} P_0 \right), \quad (\text{D5}) \\ [g_{\mathbf{q}}(\mathbf{p}_0, \mathbf{q}_0)]_{\alpha, \beta} &= \frac{1}{2} \text{Tr} \left(\sigma_{\alpha} P_0 \left. \frac{\partial H}{\partial q_{\beta}} \right|_{\mathbf{p}_0, \mathbf{q}_0} P_0 \right). \end{aligned}$$

Note that the polarization vector and the effective g -tensors are basis dependent. The SU(2) transformation of the basis multiplies them with a corresponding SO(3) matrix from the left. If the transformation is only the change of the phase difference between the states, the corresponding orthogonal matrix $R_z(\varphi)$ describes a rotation around the z axis. Later, we use these basis dependent quantities to calculate the location and the susceptibility matrix of the Weyl points which are independent from the basis choice. This independence can be inferred from the formulas.

When searching for a degeneracy point $\mathbf{p}_0 + \delta\mathbf{p}$ in the vicinity of \mathbf{p}_0 , for a fixed value of $\mathbf{q}_0 + \delta\mathbf{q}$, an approximate result can be obtained by requiring that the energy gap of the effective Hamiltonian of Eq. (D4) should vanish:

$$\boldsymbol{\Delta}^{(1)} = \mathbf{0}. \quad (\text{D6})$$

The solution of this equation for $\delta\mathbf{p}$ provides the approximate position $\mathbf{p}_0 + \delta\mathbf{p}$ of the degeneracy point.

It is worth noting that the second order Schrieffer–Wolff transformation is more than the projection of a second order expansion of the Hamiltonian to its near-degenerate subspace.

2. Finding Weyl points

The Weyl points are the generic point-like degeneracies in the three dimensional configurational space (containing the points \mathbf{p}), for a fixed control parameter vector \mathbf{q}_0 . We neglect \mathbf{q}_0 in the arguments for brevity. The equation providing an approximate position of the degeneracy is that the effective Hamiltonian should vanish, i.e.,

$$H_{\text{eff}}^{(1)}(\mathbf{p}_0 + \delta\mathbf{p}) = \boldsymbol{\sigma} \cdot [\boldsymbol{\Delta}_0(\mathbf{p}_0) + g_{\mathbf{p}}(\mathbf{p}_0) \delta\mathbf{p}] = 0. \quad (\text{D7})$$

Rearranging yields

$$g_{\mathbf{p}}(\mathbf{p}_0) \delta\mathbf{p} = -\boldsymbol{\Delta}_0(\mathbf{p}_0), \quad (\text{D8})$$

which is solved using the inverse of the g -tensor

$$\delta\mathbf{p} = -g_{\mathbf{p}}^{-1}(\mathbf{p}_0) \boldsymbol{\Delta}_0(\mathbf{p}_0). \quad (\text{D9})$$

The resulting $\mathbf{p}_0 + \delta\mathbf{p}$ is not an exact Weyl point in general, but it is closer to the Weyl point than \mathbf{p}_0 . Following this scheme, we iterate the process with the following formula

$$\mathbf{p}_{n+1} = \mathbf{p}_n - g_{\mathbf{p}}(\mathbf{p}_n)^{-1} \boldsymbol{\Delta}_0(\mathbf{p}_n), \quad (\text{D10})$$

until the energy splitting is sufficiently small; in our numerics, we used the threshold of 10^{-12} GHz. The starting point \mathbf{p}_0 needs to be close to the exact Weyl point. When searching for an ordinary Weyl point with the above iteration, the effective g -tensor is non-singular throughout the iteration, as it is non-singular in the Weyl point. Hence the inverse used in the iteration of Eq. (D10) does exist.

3. Finding the nodal loop

In the presence of a nodal loop, our goal is to numerically locate a discrete set of its points that allows us to draw the loop. To achieve that, we intersect the latter with planes in the configurational space, as shown in Fig. 3b. From the initial point \mathbf{p} (see, e.g., the blue point in the $\varphi_z = 0$ plane in Fig. 3b), we restrict the displacement $\delta\mathbf{p}$ as

$$\delta\mathbf{p} = c_1 \mathbf{v}_1 + c_2 \mathbf{v}_2 = \underbrace{(\mathbf{v}_1 | \mathbf{v}_2)}_V \underbrace{\begin{pmatrix} c_1 \\ c_2 \end{pmatrix}}_c, \quad (\text{D11})$$

where \mathbf{v}_1 and \mathbf{v}_2 are two arbitrary vectors in the 3D configurational space that span the plane. The condition for the Weyl point in the linearized effective Hamiltonian in Eq. (D8) changes to

$$\underbrace{g_{\mathbf{p}}(\mathbf{p}_0)}_{gV} \mathbf{c} = -\boldsymbol{\Delta}_0(\mathbf{p}_0). \quad (\text{D12})$$

At first sight this is an overdetermined linear set for c_1 and c_2 , since it contains 3 conditions but only 2 variables. However, because of the \mathcal{PT} symmetry discussed in App. C, there is a basis where the effective Hamiltonian is real-valued. In this basis, the second component of Eq. (D12) simplifies to the identity $0 = 0$, meaning that there is a unique solution for the equation.

One way to solve Eq. (D12) is to look for the vector \mathbf{c} where $|g_V \mathbf{c} + \Delta_0|^2$ is minimal. Note that at the minimum point, the minimum value is actually zero. Equating the derivative of $|g_V \mathbf{c} + \Delta_0|^2$ with respect to \mathbf{c} to zero yields

$$g_V^T g_V \mathbf{c} = -g_V^T \Delta_0. \quad (\text{D13})$$

Note that Eq. (D13) can also be obtained by multiplying Eq. (D12) with g_V^T from the left. Now we can solve Eq. (D13) using the inverse of the 2×2 matrix $g_V^T g_V$ as

$$\mathbf{c} = -(g_V^T g_V)^{-1} g_V^T \Delta_0. \quad (\text{D14})$$

Following the spirit of the iteration at the end of the previous section, the analogous iteration to find the intersection of the nodal loop and the considered plane is defined as

$$\mathbf{p}_{n+1} = \mathbf{p}_n + \delta \mathbf{p} = \mathbf{p}_n + V \mathbf{c} = \quad (\text{D15})$$

$$\mathbf{p}_n - V [V^T g_p^T(\mathbf{p}_n) g_p(\mathbf{p}_n) V]^{-1} V^T g_p^T(\mathbf{p}_n) \Delta_0(\mathbf{p}_n).$$

where we have used Eqs. (D11), (D12), and (D14).

The first point of the loop is searched in the $\varphi_z = 0$ plane. Then every starting point searching the points of the nodal loop is 0.01 rad distance in the tangential direction of the nodal loop from the previous point. The search is restricted to the plane perpendicular to the step (Fig. 3). The tangent vector \mathbf{v} of the nodal loop is determined by the g -tensor as $g_p \mathbf{v} = 0$, which means that the splitting is zero in the linear order in that direction.

4. Susceptibility matrix of ordinary Weyl points

Here, we express the motional susceptibility matrix χ introduced in Eq. (4) of the main text with the configurational- and control-space effective g -tensors g_p and g_q , respectively. The susceptibility matrix χ describes the motion of the Weyl points in the configurational parameter space \mathbf{p} upon changing the control parameters \mathbf{q} . The linear effective Hamiltonian expanded at a Weyl point does not have a constant term:

$$\Delta^{(1)}(\mathbf{p}, \mathbf{q}) = g_p(\mathbf{p}_0, \mathbf{q}_0) \delta \mathbf{p} + g_q(\mathbf{p}_0, \mathbf{q}_0) \delta \mathbf{q}. \quad (\text{D16})$$

The condition for Weyl points reads $\Delta^{(1)} = 0$. Rearranging this equation and acting with g_p^{-1} from the left gives

$$\delta \mathbf{p} = -(g_p^{-1} g_q) \delta \mathbf{q} = \chi(\mathbf{p}_0, \mathbf{q}_0) \delta \mathbf{q}, \quad (\text{D17})$$

which determines the linear order displacement $\delta \mathbf{p}$ of the Weyl point for the arbitrary perturbation $\delta \mathbf{q}$ in the control space, which is in fact the definition of the susceptibility matrix.

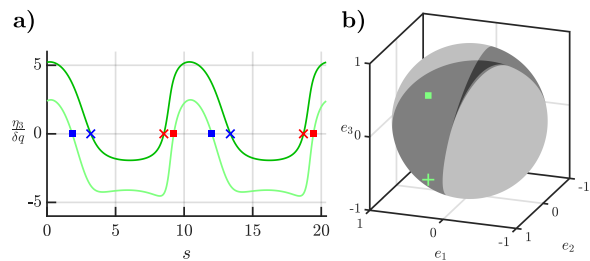


FIG. 4. **Survivor Weyl points of the broken nodal loop.** a) The zeros of the function $\eta_3(s)$ (third component of right hand side of Eq. (E4)) determines where the survivor Weyl points are located for an infinitesimal perturbation. For perturbations in different directions of the control space, the function $\eta_3(s)$ is different, causing the Weyl-point teleportation. b) The direction of the perturbation also determines the number of the survivor Weyl points. The pale gray region has no Weyl points, the medium gray has 4 Weyl points and the dark grey region has 8 Weyl points. The perturbations used in the main text is in the 4-point region. For both markers (square, cross) in b), the arc length parameters of the survivor Weyl points are depicted by the same markers on a).

Notice that the susceptibility matrix is independent from the choice of basis in the two-fold degenerate eigenspace at the Weyl point. Changing the basis multiplies the g -tensors g_p and g_q with the same orthogonal matrix from the left, and this exactly cancels out in the expression $g_p^{-1} g_q$.

Appendix E: Survivor Weyl points close to the transition point

In this section, we derive the location of the Weyl points that ‘survive’ upon an infinitesimal perturbation of a nodal loop. Moreover, we show that the number of survivor Weyl points depends on *how* the nodal loop is perturbed: for the example considered, the number of survivor Weyl points is either 0, 4, or 8.

The nodal loop $\mathbf{p}_0(s)$ in the configurational parameter space can be parametrized by its arc length s and its vicinity can be parametrized by the $\delta \mathbf{p}_\perp$ perpendicular displacement from the nodal loop. The perturbed effective Hamiltonian reads

$$\Delta^{(1)} = g_p(s) \delta \mathbf{p}_\perp + g_q(s) \delta \mathbf{q}, \quad (\text{E1})$$

where we omitted the \mathbf{q}_0 -dependence in the arguments of the g -tensors for simplicity because the nodal loop corresponds to only specific discrete \mathbf{q}_0 values. The survivor Weyl points are located at the arc length parameter s where the condition

$$\Delta^{(1)} = 0 \quad (\text{E2})$$

has solution for $\delta \mathbf{p}_\perp$. The $g_p(s)$ configurational-space effective g -tensor is a singular matrix for the points of the

nodal loops, hence we can not solve Eq. (E2) using the inverse of it. Instead, we use the singular value decomposition of $g_{\mathbf{p}}(s)$ to rewrite Eq. (E2) as

$$U(s)\Sigma(s)V(s)^{-1}\delta\mathbf{p}_{\perp} = -g_{\mathbf{q}}(s)\delta\mathbf{q} \quad (\text{E3})$$

$$\Sigma(s)\underbrace{V(s)^{-1}\delta\mathbf{p}_{\perp}}_{\delta\tilde{\mathbf{p}}_{\perp}} = -\underbrace{U(s)^{-1}g_{\mathbf{q}}(s)\delta\mathbf{q}}_{\boldsymbol{\eta}(s,\delta\mathbf{q})} \quad (\text{E4})$$

where $\Sigma = \text{diag}(\Sigma_1, \Sigma_2, 0)$ is a diagonal matrix and U and V are 3×3 orthogonal matrices. The third column of Σ is zero, therefore the third component of the left hand side is also zero. Therefore, the third component of Eq. (E4), that is,

$$\eta_3(s_0, \delta\mathbf{q}) = 0, \quad (\text{E5})$$

can be used to find the arc length parameters s_0 where Weyl points appear upon applying the perturbation $\delta\mathbf{q}$. It is worth noting that $\boldsymbol{\eta}(s, \delta\mathbf{q})$ is independent of the

choice of the basis of the two-dimensional degenerate subspace at the Weyl point. The first-order perpendicular-to-nodal-loop of the survivor Weyl points is given as

$$\delta\mathbf{p}_{\perp} = -g_{\mathbf{p}}^+(s_0(\delta\mathbf{q}))g_{\mathbf{q}}(s_0(\delta\mathbf{q}))\delta\mathbf{q}, \quad (\text{E6})$$

where $g_{\mathbf{p}}^+ = V\Sigma^+U^{-1}$ is the Moore–Penrose inverse of the g -tensor with $\Sigma^+ = \text{diag}(\Sigma_1^{-1}, \Sigma_2^{-1}, 0)$. There is also a first-order parallel-to-nodal-loop motion of the survivor Weyl points, but determining that requires a second order calculation.

This derivation indicates the Weyl-point teleportation: for infinitesimal perturbations $\delta\mathbf{q}$ in different directions the function $\eta_3(s, \delta\mathbf{q})$ has roots at different arc length values (see Fig. 4a), meaning that different points of the nodal loop survive. For infinitesimally small perturbations $\delta\mathbf{q} = \mathbf{n}\delta q$ only the direction \mathbf{n} describes the location of the surviving Weyl points. Their number also depends on the direction of the perturbation which gives a phase diagram on the unit sphere (see Fig. 4b).